Brain virtual histology with X-ray phase-contrast tomography Part II: 3D morphologies of amyloid-β plaques in Alzheimer's disease models

Matthieu Chourrout, Margaux Roux, Carlie Boisvert, Coralie Gislard, David Legland, Ignacio Arganda-Carreras, Cécile Olivier, Françoise Peyrin, Hervé Boutin, Nicolas Rama, et al.

Research Article Vol. 13, No. 3 / 1 Mar 2022 / Biomedical Optics Express 1640
Biomedical Optics EXPRESS

Brain virtual histology with X-ray phase-contrast tomography Part II: 3D morphologies of amyloid-β plaques in Alzheimer's disease models

MATTHIEU CHOURROUT,[1] MARGAUX ROUX,[1] CARLIE BOISVERT,[1,15] CORALIE GISLARD,[1] DAVID LEGLAND,[2] IGNACIO ARGANDA-CARRERAS,[3,4,5] CÉCILE OLIVIER,[6] FRANÇOISE PEYRIN,[6] HERVÉ BOUTIN,[7] NICOLAS RAMA,[8] THIERRY BARON,[9] DAVID MEYRONET,[10] EMMANUEL BRUN,[11] HUGO ROSITI,[12] MARLÈNE WIART,[13,14,16] AND FABIEN CHAUVEAU[1,14,16,*]

[1]*Univ. Lyon, Lyon Neuroscience Research Center, CNRS UMR5292, Inserm U1028, Université Claude Bernard Lyon 1, Lyon, France*
[2]*UR BIA; BIBS Facility, INRAE, Nantes, France*
[3]*University of the Basque Country (UPV/EHU), San Sebastian, Spain*
[4]*Ikerbasque, Basque Foundation for Science, Bilbao, Spain*
[5]*Donostia International Physics Center (DIPC), San Sebastian, Spain*
[6]*Univ. Lyon, CREATIS; CNRS UMR5220; INSERM U1044; INSA-Lyon; Univ. Lyon 1, Lyon, France*
[7]*Univ. Manchester, Faculty of Biology Medicine and Health, Wolfson Molecular Imaging Centre, Manchester, UK*
[8]*Univ. Lyon, CRCL; INSERM U1052; CNRS UMR5286; Univ. Lyon 1; Centre Léon Bérard, Lyon, France*
[9]*Univ. Lyon, ANSES, Lyon, France*
[10]*Univ. Lyon, Hospices Civils de Lyon, Lyon, France*
[11]*Univ. Grenoble Alpes, Inserm UA07 Strobe Grenoble, France*
[12]*Univ. Clermont Auvergne, Institut Pascal; CNRS UMR 6602; SIGMA Clermont, Clermont-Ferrand, France*
[13]*Univ. Lyon, CarMeN Laboratory; INSERM U1060; INRA U1397; Hospices Civils de Lyon, Lyon, France*
[14]*CNRS, Lyon, France*
[15]*Current affiliation: Faculty of Medicine, The Ottawa Hospital and University of Ottawa, Ottawa, Ontario, Canada*
[16]*These authors contributed equally to this work*
[*]*chauveau@cermep.fr*

Abstract: While numerous transgenic mouse strains have been produced to model the formation of amyloid-β (Aβ) plaques in the brain, efficient methods for whole-brain 3D analysis of Aβ deposits have to be validated and standardized. Moreover, routine immunohistochemistry performed on brain slices precludes any shape analysis of Aβ plaques, or require complex procedures for serial acquisition and reconstruction. The present study shows how in-line (propagation-based) X-ray phase-contrast tomography (XPCT) combined with ethanol-induced brain sample dehydration enables hippocampus-wide detection and morphometric analysis of Aβ plaques. Performed in three distinct Alzheimer mouse strains, the proposed workflow identified differences in signal intensity and 3D shape parameters: 3xTg displayed a different type of Aβ plaques, with a larger volume and area, greater elongation, flatness and mean breadth, and more intense average signal than J20 and APP/PS1. As a label-free non-destructive technique, XPCT can be combined with standard immunohistochemistry. XPCT virtual histology could thus become instrumental in quantifying the 3D spreading and the morphological impact of seeding when studying prion-like properties of Aβ aggregates in animal models of Alzheimer's disease. This is Part II of a series of two articles reporting the value of in-line XPCT for virtual histology of the brain; Part I shows how in-line XPCT enables 3D myelin mapping in the whole

#438890 https://doi.org/10.1364/BOE.438890
Journal © 2022 Received 27 Jul 2021; revised 8 Oct 2021; accepted 12 Oct 2021; published 23 Feb 2022

Biomedical Optics EXPRESS

rodent brain and in human autopsy brain tissue.

1. Introduction

The amyloid cascade is considered pivotal in the development of Alzheimer's disease. In the last 20 years, numerous transgenic mouse strains have been produced to model the accumulation of amyloid-β (Aβ) peptides and formation of Aβ plaques in the brain. Most are knock-in animals, obtained by insertion of human genes, which usually include mutations observed in familial cases: presenilins (PSEN1/2), amyloid precursor protein (APP), microtubule associated protein tau (MAPT), triggering receptor expressed on myeloid cells 2 (TREM2), etc. The Alzforum database currently lists 126 mouse models with 1 transgene, and 62 multi-transgene mouse models (https://www.alzforum.org/research-models; last access on October 14, 2021). Fast methods for whole-brain analysis are thus of great value for characterizing and comparing phenotypes among the variety of strains available. Several recent developments have been proposed to enable individual Aβ plaque detection through the entire brain in 3D. These include two-photon serial imaging [1], ultramicroscopy [2], or optical projection tomography [3], which all belong to the field of optical mesoscopy.

X-ray-based virtual histology is a new field of research mainly aimed at 3D datasets of biological tissue virtually sliced in any direction [4]. X-ray phase-contrast tomography (XPCT) using synchrotron radiation allows imaging of excised biological tissues or organs with weak X-ray absorption (like the brain) at microscopic level [5]. XPCT achieves a high signal-to-noise ratio without the need to add staining agents, by probing small changes in refractive indices in the tissue microstructure. It provides micrometric spatial resolution and isotropic reconstruction in a $\sim$ 1 cm^3 field of view (FOV), thus offering ideal prerequisites for imaging protein aggregates of $\sim$ 10 μm in the entire and intact (unsliced, unstained) mouse brain [6].

Several pioneer studies already reported detection of Aβ plaques with various X-ray phase-contrast techniques [7–9]. However, these first developments required long acquisition times (30 min–180 min) and/or provided limited anatomical contrast. Recently, free space propagation between object and detector has been shown to be a simple, fast and efficient technique for detecting Aβ plaques with good contrast [10,11]. In addition, anatomic contrast can be greatly enhanced by dehydrating the brain prior to imaging, which increases small local differences between the refractive indices of the different brain structures [5,6]. In terms of analysis and quantification, most previous studies reported only qualitative results, or quantification restricted to parameters accessible to standard 2D histology (e.g., number of plaques, diameter, volume). Only one recent report used XPCT to extract sphericity of Aβ plaques inside the cerebellum [12]. The present study aimed to realize the full potential of XPCT by combining:

1. optimal brain tissue preparation through dehydration in ethanol,
2. fast acquisition in three different (mono, double and triple) transgenic mouse strains displaying Aβ pathology,
3. semi-automatic segmentation of Aβ plaques inside the hippocampus using open-source tools (combination of Fiji plugins),
4. and full characterization of their 3D morphology.

This is Part II of a series of two articles reporting the value of in-line XPCT for virtual histology of the brain; Part I shows how in-line XPCT enables myelin mapping of the whole brain [13].

Biomedical Optics EXPRESS

2. Methods

2.1. Samples

All experimental procedures were carried out in accordance with European regulations for animal use (EEC Council Directive 2010/63/EU). The present study was performed on excised brains. Three transgenic lines were used, for a total of 8 brains:

1. mono-transgene line J20 (n=2 animals, 2 y.o.), with mutant APP [14];
2. double-transgene line APPswe/PSEN1dE9 or APP/PS1 (n=3 animals, 1 y.o.), with mutant APP and mutant PSEN1 [15];
3. triple-transgene line 3xTg (n=3 animals, 1 y.o.), with mutant APP, mutant PSEN1 and mutant MAPT [16].

One additional brain, from a wild-type mouse of C57BL6/129sv background, was used as a control.

2.2. Preparation

On the day before imaging, formaldehyde-fixed brains were dehydrated in baths of ascending ethanol concentrations (25, 50, 75, 96%, at least 5 min per bath), and conditioned in plastic tubes (1 cm diameter) filled with ethanol.

2.3. Acquisition

Imaging was performed at the ID19 beamline of the European Synchrotron Research Facility (ESRF, Grenoble, France). Acquisition parameters and data characteristics are summarized in Table 1. Briefly, the tomographic images were recorded within 3 minutes at a single sample-detector distance where the camera was positioned away from the sample (3 m) to obtain phase contrast. The experiments were performed with a polychromatic "pink" incident X-ray beam of 26 keV energy. Tomographic reconstructions were performed using the single-distance phase-retrieval approach ("Paganin" method [17]) with PyHST2 software [18], the δ/β ratio being set to 1000.

2.4. Segmentation

Semi-automated detection of Aβ plaques used Fiji software [19]. A pipeline was built with the following plugins: segmentation editor (to isolate hippocampus; https://imagej.net/Segmentation_Editor), Trainable Weka Segmentation 3D (to identify plaques) [20], and MorphoLibJ [21] and 3D ImageJ suite [22] (to label objects and extract relevant parameters). Image features used for trainable segmentation were "Difference of Gaussian", "Variance", and "Maximum" for J20 and 3xTg. For APP/PS1, "Minimum" was used instead of "Maximum" after the application of a 3D Laplacian-of-Gaussian (Mexican Hat) filter [23], as suggested by Astolfo et al. [10]. A step-by-step guide to perform all image processing, "Amyloid-β XPCT Workflow", is publicly available (DOI: 10.5281/zenodo.4584752) [24].

2.5. 3D parameters

Sphericity, elongation, flatness, sparseness and distance to nearest object were outputs from 3D ImageJ Suite. Surface area, volume, mean breadth and mean signal intensity (here normalized by background intensity) were outputs from MorphoLibJ. Definitions of these parameters are reported in Table 2.

Biomedical Optics EXPRESS

Table 1. Acquisition parameters and data characteristics.

Setup	ID19
Detector	sCMOS (PCO edge)
Scintillator	LuAg (500 µm)
Energy [keV]	26
Sample-detector distance [m]	3
Exposure time [s]	0.04
Number of projections	3000
Sample rotation [°]	360
Acquisition time [min]	3
Reconstruction algorithm	PyHST 2 (Paganin filter, δ/β = 1000)
Field-of-view [cm^3]	$1.3 \times 1.3 \times 0.9$
Matrix	2048×2048
Number of slices	1400
Voxel size (isotropic) [µm]	6.5
Image size [GB]	11.7 (as 16-bit data)
Estimated dose [Gy]	35000

2.6. Analysis and statistics

Prism 8 (GraphPad) was used for violin plots and statistics. The Welch version of one-way ANOVA (gaussian populations, unequal variances) was used to compare the above-cited parameter values of individual Aβ plaques across the three transgenic groups, with additional Games-Howell tests (recommended for n>50) for pairwise comparisons. Linear correlations between parameters were quantified on Pearson correlation coefficient. MIPAV (v10.0.0, CIT, NIH [26]) was used for 2D visualization of semi-transparent overlay of plaque labels onto native images. Amira Software 6 (ThermoFisher) was used for all 3D renderings.

2.7. Immunochemistry

One sample of each transgenic strain underwent paraffin embedding, 7 μm-thick microtome slicing (Leica RM2245) and standard Aβ immunofluorescence or histological staining. Aβ immunofluorescence was performed after i) standard dewaxing, ii) antigen retrieval with 100% formic acid for 15–20 minutes at room temperature (RT), and iii) blocking with 5% Bovine Serum Albumin (BSA) and 0.5% Triton-X in Phosphate Buffer Saline (PBS, Sigma-Aldrich ref. P4417) for 30 minutes at RT, by incubating the anti-Aβ monoclonal antibody 4G8 (Covance, ref. SIG-39220, dilution 1 : 1000 in 5% BSA) on each microscope slide overnight, in a humid chamber at 4°C. After three 5 min washes in PBS at RT, secondary antibody (anti-mouse AlexaFluor 488 or 546, ThermoFisher, dilution 1 : 500 in 5% BSA) was incubated on each microscope slide for 60 minutes, in a humid chamber at RT. After three 5 min washes in PBS at RT, slides were mounted with DAPI-containing medium (Roti-Mount FluorCare DAPI, Carl Roth), and stored at 4°C. Thioflavin S staining (ThS, Sigma-Aldrich ref. T1892) (0.05% in ethanol 70%) was performed for 10 min at RT after dewaxing, and slides were mounted with DAPI-containing medium, after two 1 min washes in ethanol 70%. Fluorescence images were captured on a microscope (AxioScope A1, Zeiss) equipped with a digital camera interfaced with image-analysis software (ZEN 2 lite, Zeiss).

Biomedical Optics EXPRESS

Table 2. Morphometric parameters. More details are available at https://imagej.net/MorphoLibJ.html#Documentation and in [25].

Name	Definition	Formula
Compactness *(not reported)*	Ratio (C) between volume (V) and surface area (A); "3D ImageJ Suite" implements a 'discrete' compactness, described by Bribiesca (2008), estimated from the number of voxels (N_{voxels}); spheres have a compactness of 1.	$C = \frac{36\pi V^2}{A^3} \approx \frac{N_{voxels} - \frac{A}{6}}{N_{voxels} - (N_{voxels})^{2/3}}$
Sphericity	Ratio (S) between volume (V) and surface area (A); linked to compactness (or discrete compactness); spheres have a sphericity of 1.	$S = C^{1/3} \approx \left(\frac{N_{voxels} - \frac{A}{6}}{N_{voxels} - (N_{voxels})^{2/3}} \right)^{1/3}$
Elongation	Elongation of the equivalent ellipsoid, where $R_1 >= R_2 >= R_3$ are are the lengths of the semi-axes of the ellipsoid with same inertia tensor as the object	$Elongation = \frac{R_1}{R_2}$
Flatness	Flatness of the equivalent ellipsoid, where $R_1 >= R_2 >= R_3$ are are the lengths of the semi-axes of the ellipsoid with same inertia tensor as the object	$Flatness = \frac{R_2}{R_3}$
Sparseness	Ratio between the volume of the equivalent ellipsoid (V_{ell}) and the volume of the object (V_{obj})	$Sparseness = \frac{V_{ell}}{V_{obj}}$
Mean Signal Intensity (SI)	Mean intensity from the raw image; here reported as a mean signal-to-background ratio	
Volume	Volume in the given unit (μm^3)	
Surface Area	Surface area in the given unit (μm^2)	
Mean Breadth	Average of the Feret diameter of convex objects measured over a selected number of orientations (µm)	
Distance	Distance between two closest segmented objects (µm)	

Biomedical Optics EXPRESS

3. Results

3.1. Qualitative analysis

After ethanol dehydration, brain anatomy, and specifically white matter tracts, was uniquely displayed on XPCT images (Fig. 1), as reported in Part I of this series of articles [13].

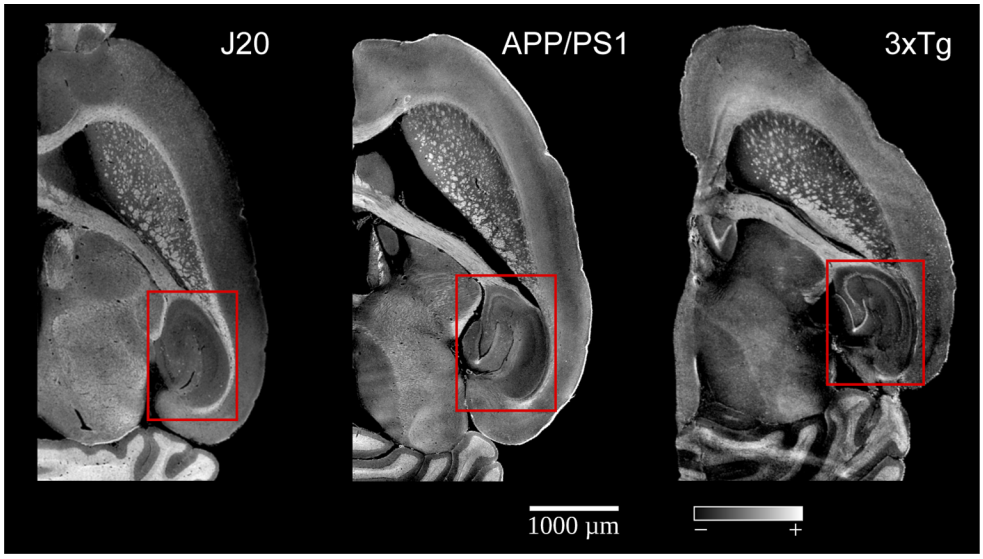

Fig. 1. Whole-brain anatomy of ethanol-dehydrated brains from the three mouse strains (XPCT single slices). The plaques from the three strains are visible mainly in the hippocampi (in red).

One additional formaldehyde-fixed sample of the J20 strain was scanned in PBS using the same set-up and reconstruction algorithm (Fig. S1): though some Aβ plaques were visible, surrounding brain tissue exhibited low overall signal intensity, strongly contaminated by ring artefacts. Thus, imaging in ethanol was required for region-specific segmentation. In this proof-of-concept study, we chose to focus on the hippocampus, in which all three mouse strains exhibited Aβ plaques. However, these plaques displayed strikingly different appearances (Fig. 2): i) J20 exhibited numerous small intense spots, sometimes very close to each other and seemingly

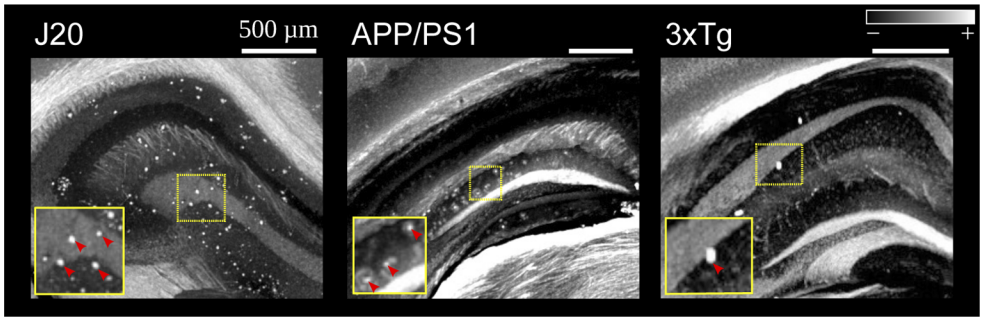

Fig. 2. XPCT images (maximum intensity projections over 50 slices) obtained at the level of the dorsal hippocampus, showing the density and appearance of Aβ plaques in the three mouse strains.

Biomedical Optics EXPRESS

coalescing; ii) APP/PS1 displayed intense spots, often surrounded by a diffuse rim, resembling typical human dense-core plaques; iii) 3xTg showed few but large and highly intense deposits.

These 3D signals obtained without labeling matched the 2D fluorescence of corresponding brain slices after thioflavin S staining or Aβ-peptide immunohistochemistry (Fig. 3), although some of the stained plaques seemed not to produce hyperintense contrast on XPCT.

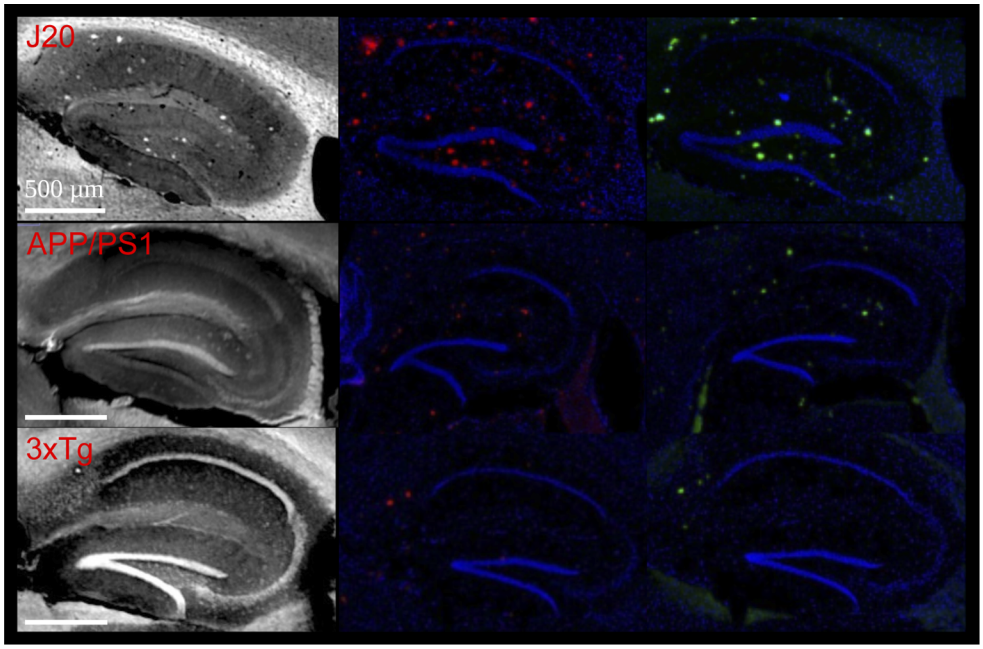

Fig. 3. Corresponding XPCT image (left row), amyloid staining with 4G8 antibody (red filter, exc 550 nm, em 605 nm), and Thioflavin S staining (right row, green filter, exc 485 nm, em 515 nm), for the three transgenic mouse strains. DAPI staining was obtained with a blue fluorescence filter (exc 365 nm, em 445 nm).

3.2. Morphological quantification

Following hippocampus extraction (steps 2–3 in the Amyloid-β XPCT Workflow), machine learning was used to perform Aβ plaque recognition: Trainable Weka Segmentation 3D used a strain-selective classifier that was built from 5 consecutive slices and then applied to the whole hippocampus (>200 slices) to produce a probability map that was thresholded by visual inspection (steps 4–5 in the Amyloid-β XPCT Workflow). This strategy proved versatile and accommodated the different types and numbers of plaques imaged in this study (Fig. 4).

After automatic labeling and size filtering of segmented objects (step 6 in the Amyloid-β XPCT Workflow), a few manual cleaning steps were performed under expert supervision (author FC). False-positive objects were, in most cases, located in the myelinated tracts of the perforant pathway (Fig. S2). On rare occasions, neurons or blood clots remaining in vessels were also detected as plaques. In 3xTg brains, a few false-positive labels were easily identified and removed, out of a dozen correctly segmented plaques (6–16 per hemisphere). In J20, which in contrast had several hundreds of plaques (774–916 per hemisphere), expert screening showed that the false-positive detection rate was below 5%. Importantly, not all J20 plaques could be individually separated; hence some segmented objects were "twin" plaques, in close contact, which were manually removed from analysis. In the case of APP/PS1, plaques were of lower signal intensity, and could not be unambiguously distinguished from perforant pathway signals. APP/PS1 volumes

Biomedical Optics EXPRESS

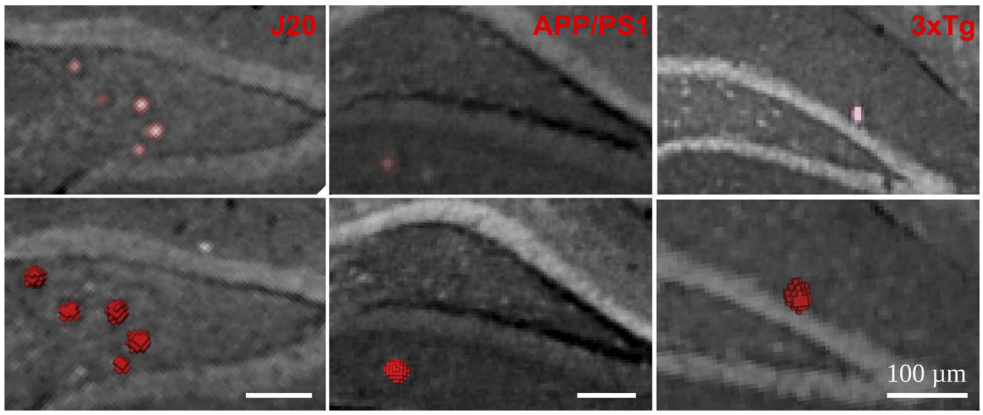

Fig. 4. Representative 2D overlay and 3D orthographic rendering (AMIRA) of segmented plaques for each strain.

were thus screened to manually select a hundred representative plaques outside the perforant tracts, which were used to calculate morphological parameters. Finally, as a specificity control, the 3 classifiers were applied to the hippocampus of a wild-type mouse, and, after similar

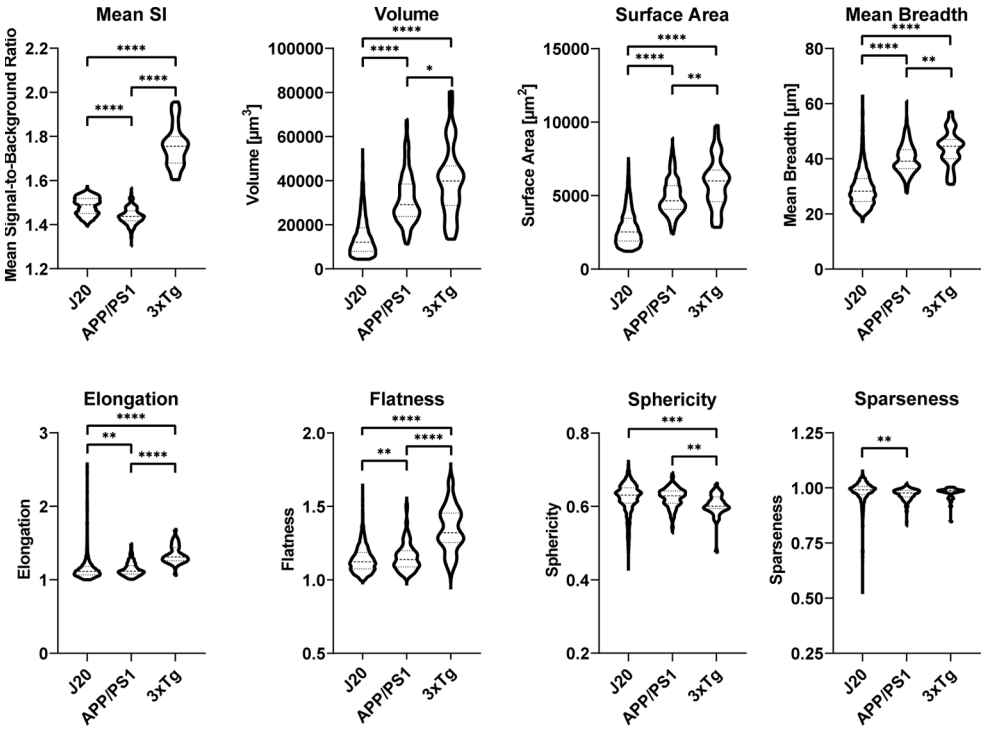

Fig. 5. Violin plots of morphological parameters extracted from the population of Aβ plaques. Definitions of the parameters are reported in Table 2; Significance levels of pairwise Games-Howell comparisons are indicated (* $p<0.05$; ** $p<0.01$; *** $p<0.001$; **** $p<0.0001$); Mean (interquartile range) are represented as dashed lines.

Biomedical Optics EXPRESS

thresholding and size filtering, yielded no other detection than the same type of false-positive objects described above (Fig. S2).

Both the MorphoLibJ and 3D ImageJ Suite plugins were able to extract morphological parameters (step 7 in the Amyloid-β XPCT Workflow), and we here report a combination of the shape parameters available for each strain (Fig. 5).

As expected from visual assessment, 3xTg displayed the highest plaque signal intensity after normalization to background (3xTg > J20 > APP/PS1, $p<0.0001$), while J20 had the smallest volume (J20 < APP/PS1 < 3xTg, $p<0.0001$) and surface area (J20 < APP/PS1 < 3xTg, $p<0.0001$) per plaque. Mean breadth, a parameter proportional to the integral of the mean curvature, was also significantly less in J20 (< APP/PS1 < 3xTg, $p<0.0001$). Shape differences were more pronounced for 3xTg, which had greater elongation and flatness (3xTg > APP/PS1 ≈ J20, both $p<0.0001$), and lower sphericity (3xTg < APP/PS1 ≈ J20, $p = 0.0002$) compared to J20 and APP/PS1. Finally, it was possible to compute nearest-neighbor distances (Fig. S3), the mean value of which was 4-fold greater in 3xTg than J20. These parameters are not mutually independent, and correlation matrices were computed to highlight strain differences in correlation coefficients (Fig. 6).

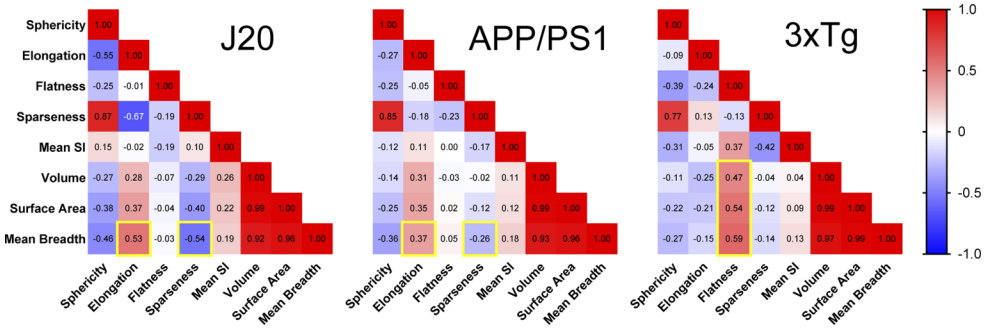

Fig. 6. Pearson r correlation coefficients (color-coded from −1 = blue to 1 = red) between the 8 parameters. Correlation coefficients highlighted with yellow boxes refer to comments in the text.

While sphericity and sparseness were highly correlated in all three strains, mean breadth was positively correlated with elongation, and negatively with sparseness, both in J20 and APP/PS1 (Fig. 6, yellow boxes), but not in 3xTg. In contrast, flatness was correlated with surface area, volume and mean breadth in 3xTg only (Fig. 6, yellow boxes).

4. Discussion

The present study went beyond previous pioneer reports of Aβ detection with XPCT by:

1. studying a complete experimental group (10 brains in total vs 1–2 samples);
2. comparing 3 different strains (vs. a single one);
3. and providing access to multiple morphometric parameters (while previous reports were confined to plaque number, volume and sphericity).

An additional contribution consisted in building and sharing a "biologist-friendly" analysis workflow, by assembling multiple Fiji plugins: segmentation editor, Trainable Weka Segmentation, 3D, MorphoLibJ, 3D ImageJ Suite. We were especially interested in the ability of the workflow to correctly detect a significant proportion of Aβ plaques with very different appearances and morphologies. Hence versatility rather than completeness of the segmentation was the primary

Biomedical Optics EXPRESS

goal of the method. We were able to successfully segment numerous Aβ plaques, even when their refractive indices (and subsequent XPCT signals) were barely different from surrounding tissue, as in the case of APP/PS1. In future studies in a dedicated mouse strain, segmentation may be improved, by building a dedicated Weka classifier combining a few slices from different animals, and/or by using several classes of objects to better discriminate Aβ plaques from neuronal tracts, and/or by using wild-type littermate brains to avoid false-positive detections and thus avoid human intervention to threshold probability maps and exclude false positives.

Tested on three different transgenic mouse strains, the analysis workflow yielded an entirely new class of 3D parameters, with distribution easily measured on multiple plaques. We provide basic examples of how to handle this set of parameters: e.g., building correlation matrices (Fig. 6) or searching for spatial patterns (Visualization 1 showing the distribution of mean breadth values on APP/PS1 hippocampus). Hence, the present work leveraged 3D analysis to extract multiple morphological parameters of Aβ plaques which otherwise require extended serial microscopy acquisitions with 3D reconstruction [1]. The development of such quantification pipelines is a necessary step for popularizing XPCT in neuroscience laboratories which need to phenotype transgenic animal cohorts. Moreover, this imaging modality could be instrumental in studying the prion-like properties of Aβ fibrillar aggregates. Typical experiments involve exogenously inoculated Aβ seeds (prion-like agents) which template and accelerate Aβ deposition in the host brain [27,28]. Hence non-destructive 3D imaging would be a great advantage in identifying the spreading routes of inoculated seeds [29]. Moreover, it was suggested that seed morphology influences the final morphology of disseminated Aβ deposits; but the existence of these "morphotypes" was inferred from 2D immunohistochemistry [30] and awaits 3D confirmation.

In this proof-of-concept report, 3xTg displayed a different type of Aβ plaque, with larger volume and area, greater elongation and flatness, and much higher signal intensity than J20 and APP/PS1. Aβ aggregation has been shown to start intracellularly in hippocampal neurons of the 3xTg strain, and it is interesting to note that neuronal bodies in the hippocampus showed high signal intensity in comparison to other strains (Fig. 1). Thus, the distinct aggregation cascade in this strain might translate into different extracellular morphotypes of Aβ plaque. While the mechanisms leading to these particularities remain elusive, these observations illustrate how XPCT can probe the pathophysiological microenvironment of brain tissue. In terms of morphometry, the study identified mean breadth as an original and discriminating parameter. Mean breadth is a quantity proportional to the integral of mean curvature over area (>0 for convex objects such as Aβ plaques). In this case, mean breadth can be defined as the average of the Feret diameter measured over a selected number of orientations. It correlated strongly with area and volume (all related to the size of the plaque), but exhibited radically different correlation patterns with other parameters in 3xTg (Fig. 6). This shows that the analysis of 3D geometry can benefit from other parameters in addition to the often-reported sphericity and volume. Ultimately, the combination of all parameters results in "morphological signatures" that allows discriminating the strains. The interpretation of the associations between the morphological parameters could however complexify when the number of parameters increases. In that case, exploratory data analysis such as dimensionality reduction or clustering could help reveal which parameters correlate, and which ones carry complementary information [31,32]

Though the pathophysiological relevance of Aβ shape remains unknown, the morphology of Aβ plaques gained interest with the recent development of brain clearing techniques [2,3,33,34]. In comparison, XPCT has the following advantages: i) ultra-fast sample preparation (around 1 hour, whereas 3D immunofluorescence typically requires several days' incubation with anti-amyloid antibodies), ii) variation in size through sole ethanol dehydration (up to 40% decrease in the brain [35]) whereas most clearing techniques drastically change brain size, leading to shrinkage or expansion, through multiple and successive chemical treatments [36], and iii)

Biomedical Optics EXPRESS

whole-brain acquisition (whereas light-sheet imaging usually requires multiple acquisitions and fastidious stitching procedures). Therefore, XPCT can be positioned as a forefront technique, allowing high-throughput brain screening, and guidance for subsequent brain clearing and 3D immunohistochemistry on selected samples. XPCT is therefore unique as a whole-brain, label-free method for ex vivo amyloid imaging. The current limitations of XPCT are the following.

1. The sensitivity of detection of Aβ plaques likely depends on size and location in the brain; this point could be addressed by more precisely adjusting tissue dehydration (by varying the percentage of ethanol) so as to get minimal anatomical contrast while preserving Aβ detectability.

2. Not all Aβ plaques seem detectable and the source of the XPCT contrast from Aβ plaques is not currently fully understood, though it is likely to arise from a local change in refractive index due to insoluble fibrillar Aβ [37], along with a possible contribution of endogenous metals entrapped in the plaque [38]. Indeed, there are scarce reports of calcium accumulation in transgenic mice and in Alzheimer patients [39,40]. Furthermore, using various methods, metals like iron, copper or zinc have been shown to accumulate in amyloid plaques, although contrasting results have been reported according plaque types (mouse or human, senile or diffuse) [38,40–43]

3. The availability of synchrotron sources with XPCT capacity is restricted to 20-30 sites in the world; but several methods have been proposed to obtain phase-contrast images from a laboratory X-ray source [40,44–46].

5. Conclusion

In summary, we presented a complete workflow for ex vivo whole-brain imaging and quantification of Aβ pathology. Sample preparation was limited to reversible dehydration of tissue, which remained available for standard immunohistochemistry. Propagation-based XPCT produced unequalled image quality (Fig. S4), with various concurrent types of anatomical information (white matter, vessels, neuronal organization). New 3D parameters, not attainable on routine immunohistochemistry, were successfully extracted from 3 transgenic Alzheimer's disease models.

Funding. European Synchrotron Research Facility (ESRF) ((LS2292, MD1018, IN1041)); Labex (ANR-11-LABX-0063); Agence Nationale de la Recherche (ANR-11-IDEX-0007, NanoBrain (ANR15-CE18-0026)); Mitacs (Globalink [travel grant for Carlie Boisvert]).

Acknowledgments. This study was performed within the framework of LABEX PRIMES (ANR-11-LABX-0063) of Université de Lyon, within the "Investissements d'Avenir" program (ANR-11-IDEX-0007) operated by the French National Research Agency (ANR). The research was in part funded by the French ANR project NanoBrain (ANR15-CE18-0026). The study was supported by the European Synchrotron Research Facility (ESRF) by allocation of beam time (LS2292, MD1018, IN1041), and the authors would like to thank ESRF local contact Lukas Helfen. Carlie Boisvert was supported by Mitacs Globalink Canada (travel grant). 3xTg and WT brains were kindly provided by Dr Catherine Lawrence of the University of Manchester. Paraffin embedding and microtome slicing were performed at the CIQLE Imaging Platform, University of Lyon, with the help of Annabelle Bouchardon and Batoule Smatti.

Authors' contributions (according to Contributor Role Taxonomy (https://casrai.org/credit/)) CRediT

- Conceptualization: MW, FC
- Data curation: MC, MR, CG, CO, EB, HR
- Formal analysis: MC, MR
- Funding acquisition: FP, HR, MW, FC
- Investigation: MC, MR, CB, CG, CO
- Methodology: EB, HR, MW, FC
- Project administration: MW, FC
- Resources: DL, IAC, HB, NR, TB, DM

Biomedical Optics EXPRESS

- Supervision: EB, HR, MW, FC
- Validation: MC, FC
- Visualization: MC, MR, CB, CG
- Writing — original draft: FC
- Writing — review & editing: MC, MR, CB, EB, HR, MW, FC

Disclosures. The authors declare no conflicts of interest.

Data availability. The raw data required to reproduce these findings cannot be shared at this time due to the large size of the XPCT datafile, but are available on request. The image processing workflow is available on Zenodo [24].

Supplemental document. See Supplement 1 for supporting content.

References

1. J. D. Whitesell, A. R. Buckley, J. E. Knox, L. Kuan, N. Graddis, A. Pelos, A. Mukora, W. Wakeman, P. Bohn, A. Ho, K. E. Hirokawa, and J. A. Harris, "Whole brain imaging reveals distinct spatial patterns of amyloid beta deposition in three mouse models of Alzheimer's disease," J. Comp. Neurol. **527**(13), 2122–2145 (2019).
2. N. Jährling, K. Becker, B. M. Wegenast-Braun, S. A. Grathwohl, M. Jucker, and H.-U. Dodt, "Cerebral β-amyloidosis in mice investigated by ultramicroscopy," PLoS One **10**(5), e0125418 (2015).
3. D. Nguyen, P. J. Marchand, A. L. Planchette, J. Nilsson, M. Sison, J. Extermann, A. Lopez, M. Sylwestrzak, J. Sordet-Dessimoz, A. Schmidt-Christensen, D. Holmberg, D. Van De Ville, and T. Lasser, "Optical projection tomography for rapid whole mouse brain imaging," Biomed. Opt. Express **8**(12), 5637–5650 (2017).
4. J. Albers, S. Pacilé, M. A. Markus, M. Wiart, G. Vande Velde, G. Tromba, and C. Dullin, "X-ray-based 3D virtual histology-adding the next dimension to histological analysis," Mol. Imaging Biol. **20**(5), 732–741 (2018). Number: 5.
5. G. E. Barbone, A. Bravin, P. Romanelli, A. Mittone, D. Bucci, T. Gaaß, G. Le Duc, S. Auweter, M. F. Reiser, M. J. Kraiger, M. Hrabe de Angelis, G. Battaglia, and P. Coan, "Micro-imaging of brain cancer radiation therapy using phase-contrast computed tomography," Int. J. Radiat. Oncol., Biol., Phys. **101**(4), 965–984 (2018). Number: 4.
6. M. Marinescu, M. Langer, A. Durand, C. Olivier, A. Chabrol, H. Rositi, F. Chauveau, T. H. Cho, N. Nighoghossian, Y. Berthezène, F. Peyrin, and M. Wiart, "Synchrotron radiation X-ray phase micro-computed tomography as a new method to detect iron oxide nanoparticles in the brain," Mol. Imaging Biol. **15**(5), 552–559 (2013). Number: 5.
7. K. Noda-Saita, A. Yoneyama, Y. Shitaka, Y. Hirai, K. Terai, J. Wu, T. Takeda, K. Hyodo, N. Osakabe, T. Yamaguchi, and M. Okada, "Quantitative analysis of amyloid plaques in a mouse model of Alzheimer's disease by phase-contrast X-ray computed tomography," Neuroscience **138**(4), 1205–1213 (2006).
8. D. M. Connor, H. Benveniste, F. A. Dilmanian, M. F. Kritzer, L. M. Miller, and Z. Zhong, "Computed tomography of amyloid plaques in a mouse model of Alzheimer's disease using diffraction enhanced imaging," NeuroImage **46**(4), 908–914 (2009).
9. B. Pinzer, M. Cacquevel, P. Modregger, S. McDonald, J. Bensadoun, T. Thuering, P. Aebischer, and M. Stampanoni, "Imaging brain amyloid deposition using grating-based differential phase contrast tomography," NeuroImage **61**(4), 1336–1346 (2012).
10. A. Astolfo, A. Lathuilière, V. Laversenne, B. Schneider, and M. Stampanoni, "Amyloid-β plaque deposition measured using propagation-based X-ray phase contrast CT imaging," J. Synchrotron Radiat. **23**(3), 813–819 (2016).
11. L. Massimi, N. Pieroni, L. Maugeri, M. Fratini, F. Brun, I. Bukreeva, G. Santamaria, V. Medici, T. E. Poloni, C. Balducci, and A. Cedola, "Assessment of plaque morphology in Alzheimer's mouse cerebellum using three-dimensional X-ray phase-based virtual histology," Sci. Rep. **10**(1), 11233 (2020). Number: 1.
12. L. Massimi, I. Bukreeva, G. Santamaria, M. Fratini, A. Corbelli, F. Brun, S. Fumagalli, L. Maugeri, A. Pacureanu, P. Cloetens, N. Pieroni, F. Fiordaliso, G. Forloni, A. Uccelli, N. Kerlero de Rosbo, C. Balducci, and A. Cedola, "Exploring Alzheimer's disease mouse brain through X-ray phase contrast tomography: From the cell to the organ," NeuroImage **184**, 490–495 (2019).
13. M. Chourrout, H. Rositi, E. Ong, V. Hubert, A. Paccalet, L. Foucault, A. Autret, B. Fayard, C. Olivier, R. Bolbos, F. Peyrin, C. Crola-da Silva, D. Meyronet, O. Raineteau, H. Elleaume, E. Brun, F. Chauveau, and M. Wiart, "Brain virtual histology with X-ray phase-contrast tomography Part I: whole-brain myelin mapping in white-matter injury models," Biomed. Opt. Express **13**, 1620–1639 (2022).
14. L. Mucke, E. Masliah, G.-Q. Yu, M. Mallory, E. M. Rockenstein, G. Tatsuno, K. Hu, D. Kholodenko, K. Johnson-Wood, and L. McConlogue, "High-level neuronal expression of aβ1-42 in wild-type human amyloid protein precursor transgenic mice: synaptotoxicity without plaque formation," J. Neurosci. **20**(11), 4050–4058 (2000). Number: 11.
15. J. L. Jankowsky, D. J. Fadale, J. Anderson, G. M. Xu, V. Gonzales, N. A. Jenkins, N. G. Copeland, M. K. Lee, L. H. Younkin, S. L. Wagner, S. G. Younkin, and D. R. Borchelt, "Mutant presenilins specifically elevate the levels of the 42 residue β-amyloid peptide in vivo: evidence for augmentation of a 42-specific ? secretase," Hum. Mol. Genet. **13**(2), 159–170 (2004). Number: 2.
16. S. Oddo, A. Caccamo, J. D. Shepherd, M. Murphy, T. E. Golde, R. Kayed, R. Metherate, M. P. Mattson, Y. Akbari, and F. M. LaFerla, "Triple-transgenic model of Alzheimer's disease with plaques and tangles," Neuron **39**(3), 409–421 (2003). Number: 3.

Biomedical Optics EXPRESS

17. D. Paganin, S. C. Mayo, T. E. Gureyev, P. R. Miller, and S. W. Wilkins, "Simultaneous phase and amplitude extraction from a single defocused image of a homogeneous object," J. Microsc. **206**(1), 33–40 (2002). Number: Pt 1.
18. A. Mirone, E. Brun, E. Gouillart, P. Tafforeau, and J. Kieffer, "The PyHST2 hybrid distributed code for high speed tomographic reconstruction with iterative reconstruction and a priori knowledge capabilities," Nucl. Instruments Methods Phys. Res. Sect. B: Beam Interactions with Mater. Atoms **324**, 41–48 (2014).
19. J. Schindelin, I. Arganda-Carreras, E. Frise, V. Kaynig, M. Longair, T. Pietzsch, S. Preibisch, C. Rueden, S. Saalfeld, B. Schmid, J.-Y. Tinevez, D. J. White, V. Hartenstein, K. Eliceiri, P. Tomancak, and A. Cardona, "Fiji: an open-source platform for biological-image analysis," Nat. Methods **9**(7), 676–682 (2012).
20. I. Arganda-Carreras, V. Kaynig, C. Rueden, K. W. Eliceiri, J. Schindelin, A. Cardona, and H. Sebastian Seung, "Trainable Weka Segmentation: a machine learning tool for microscopy pixel classification," Bioinformatics **33**(15), 2424–2426 (2017).
21. D. Legland, I. Arganda-Carreras, and P. Andrey, "MorphoLibJ: integrated library and plugins for mathematical morphology with ImageJ," Bioinformatics **32**, 3532–3534 (2016).
22. J. Ollion, J. Cochennec, F. Loll, C. Escudé, and T. Boudier, "TANGO: a generic tool for high-throughput 3D image analysis for studying nuclear organization," Bioinformatics **29**(14), 1840–1841 (2013).
23. D. Sage, F. Neumann, F. Hediger, S. Gasser, and M. Unser, "Automatic tracking of individual fluorescence particles: application to the study of chromosome dynamics," IEEE Trans. on Image Process. **14**(9), 1372–1383 (2005).
24. M. Chourrout, M. Roux, C. Gislard, I. Arganda-Carreras, D. Legland, H. Rositi, M. Wiart, and F. Chauveau, "A Fiji pipeline to segment 3D objects and retrieve shape parameters in biomedical images," Zenodo 2021, http://10.5281/zenodo.4584752.
25. E. Bribiesca, "An easy measure of compactness for 2D and 3D shapes," Pattern Recognit. **41**(2), 543–554 (2008).
26. M. McAuliffe, F. Lalonde, D. McGarry, W. Gandler, K. Csaky, and B. Trus, "Medical image processing, analysis and visualization in clinical research," in *Proceedings 14th IEEE Symposium on Computer-Based Medical Systems. CBMS 2001*, (IEEE Comput. Soc, 2001), pp. 381–386.
27. M. Meyer-Luehmann, "Exogenous induction of cerebral -amyloidogenesis is governed by agent and host," Science **313**(5794), 1781–1784 (2006).
28. M. Friesen and M. Meyer-Luehmann, "Aβ seeding as a tool to study cerebral amyloidosis and associated pathology," Front. Mol. Neurosci. **12**, 233 (2019).
29. Y. S. Eisele, T. Bolmont, M. Heikenwalder, F. Langer, L. H. Jacobson, Z.-X. Yan, K. Roth, A. Aguzzi, M. Staufenbiel, L. C. Walker, and M. Jucker, "Induction of cerebral -amyloidosis: Intracerebral versus systemic A inoculation," Proc. Natl. Acad. Sci. **106**(31), 12926–12931 (2009).
30. J. C. Watts, C. Condello, J. Stohr, A. Oehler, J. Lee, S. J. DeArmond, L. Lannfelt, M. Ingelsson, K. Giles, and S. B. Prusiner, "Serial propagation of distinct strains of A prions from Alzheimer's disease patients," Proc. Natl. Acad. Sci. **111**(28), 10323–10328 (2014).
31. D. Legland and J. Beaugrand, "Automated clustering of lignocellulosic fibres based on morphometric features and using clustering of variables," Ind. Crop. Prod. **45**, 253–261 (2013).
32. P. J. Strzelecki, A. Swierczewska, K. Kopczewska, A. Fheed, J. Tarasiuk, and S. Wronski, "Decoding rocks: an assessment of geomaterial microstructure using X-ray microtomography, image analysis and multivariate statistics," Materials **14**(12), 3266 (2021).
33. K. Ando, Q. Laborde, A. Lazar, D. Godefroy, I. Youssef, M. Amar, A. Pooler, M.-C. Potier, B. Delatour, and C. Duyckaerts, "Inside Alzheimer brain with CLARITY: senile plaques, neurofibrillary tangles and axons in 3-D," Acta Neuropathol. **128**(3), 457–459 (2014).
34. T. Liebmann, N. Renier, K. Bettayeb, P. Greengard, M. Tessier-Lavigne, and M. Flajolet, "Three-dimensional study of Alzheimer's disease hallmarks using the iDISCO clearing method," Cell Rep. **16**(4), 1138–1152 (2016).
35. G. Rodgers, W. Kuo, G. Schulz, M. Scheel, A. Migga, C. Bikis, C. Tanner, V. Kurtcuoglu, T. Weitkamp, and B. Müller, "Virtual histology of an entire mouse brain from formalin fixation to paraffin embedding. Part 1: Data acquisition, anatomical feature segmentation, tracking global volume and density changes," J. Neurosci. Methods **364**, 109354 (2021).
36. Y. Qi, T. Yu, J. Xu, P. Wan, Y. Ma, J. Zhu, Y. Li, H. Gong, Q. Luo, and D. Zhu, "FDISCO: Advanced solvent-based clearing method for imaging whole organs," Sci. Adv. **5**(1), eaau8355 (2019).
37. M. Rak, M. R. Del Bigio, S. Mai, D. Westaway, and K. Gough, "Dense-core and diffuse Aβ plaques in TgCRND8 mice studied with synchrotron FTIR microspectroscopy," Biopolymers **87**(4), 207–217 (2007).
38. A. C. Leskovjan, A. Lanzirotti, and L. M. Miller, "Amyloid plaques in PSAPP mice bind less metal than plaques in human Alzheimer's disease," NeuroImage **47**(4), 1215–1220 (2009).
39. M. Dhenain, N. El Tannir El Tayara, T.-D. Wu, M. Guégan, A. Volk, C. Quintana, and B. Delatour, "Characterization of in vivo MRI detectable thalamic amyloid plaques from APP/PS1 mice," Neurobiol. Aging **30**(1), 41–53 (2009).
40. M. Töpperwien, F. van der Meer, C. Stadelmann, and T. Salditt, "Correlative x-ray phase-contrast tomography and histology of human brain tissue affected by Alzheimer's disease," NeuroImage **210**, 116523 (2020).
41. M. Bulk, W. M. Abdelmoula, R. J. A. Nabuurs, L. M. van der Graaf, C. W. H. Mulders, A. A. Mulder, C. R. Jost, A. J. Koster, M. A. van Buchem, R. Natté, J. Dijkstra, and L. van der Weerd, "Postmortem MRI and histology demonstrate differential iron accumulation and cortical myelin organization in early- and late-onset Alzheimer's disease," Neurobiol. Aging **62**, 231–242 (2018).

Biomedical Optics EXPRESS

42. F. Lermyte, J. Everett, J. Brooks, F. Bellingeri, K. Billimoria, P. J. Sadler, P. B. O'Connor, N. D. Telling, and J. F. Collingwood, "Emerging approaches to investigate the influence of transition metals in the proteinopathies," Cells **8**(10), 1231 (2019).
43. E. Álvarez Marimon, H. Castillo-Michel, J. Reyes-Herrera, J. Seira, E. Aso, M. Carmona, I. Ferrer, J. Cladera, and N. Benseny-Cases, "Synchrotron X-ray fluorescence and FTIR signatures for amyloid fibrillary and nonfibrillary plaques," ACS Chem. Neurosci. **12**(11), 1961–1971 (2021).
44. M. Töpperwien, M. Krenkel, D. Vincenz, F. Stöber, A. M. Oelschlegel, J. Goldschmidt, and T. Salditt, "Three-dimensional mouse brain cytoarchitecture revealed by laboratory-based x-ray phase-contrast tomography," Sci. Rep. **7**(1), 42847 (2017).
45. D. M. Paganin, H. Labriet, E. Brun, and S. Berujon, "Single-image geometric-flow X-ray speckle tracking," Phys. Rev. A **98**(5), 053813 (2018).
46. M.-C. Zdora, P. Thibault, W. Kuo, V. Fernandez, H. Deyhle, J. Vila-Comamala, M. P. Olbinado, A. Rack, P. M. Lackie, O. L. Katsamenis, M. J. Lawson, V. Kurtcuoglu, C. Rau, F. Pfeiffer, and I. Zanette, "X-ray phase tomography with near-field speckles for three-dimensional virtual histology," Optica **7**(9), 1221 (2020).